Mechanism of Antibacterial Activity via Morphology Change of α-AgVO₃: Theoretical and Experimental Insights

Regiane Cristina de Oliveira,*,† Camila Cristina de Foggi,‡ Mayara Mondego Teixeira,†
Maya Dayana Penha da Silva,† Marcelo Assis,† Eric Mark Francisco,†
Bruna Natalia Alves da Silva Pimentel,‡ Paula Fabiana dos Santos Pereira,† Carlos Eduardo Vergani,‡
Ana Lúcia Machado,‡ Juan Andres,§ Lourdes Gracia,§,∥ and Elson Longo†

†CDMF-UFSCar, Universidade Federal de São Carlos, P.O. Box 676, 13565-905 São Carlos, SP Brazil
‡FOAr-UNESP, Universidade Estadual Paulista, P.O. Box 1680, 14801903 Araraquara, SP Brazil
§Departament de Química Física i Analítica, Universitat Jaume I, 12071, Castelló de la Plana, Spain
∥Department of Physical Chemistry, University of Valencia, 46100, Burjassot, Spain

Ⓢ Supporting Information

ABSTRACT: The electronic configuration, morphology, optical features, and antibacterial activity of metastable α-AgVO₃ crystals have been discussed by a conciliation and association of the results acquired by experimental procedures and first-principles calculations. The α-AgVO₃ powders were synthesized using a coprecipitation method at 10, 20, and 30 °C. By using a Wulff construction for all relevant low-index surfaces [(100), (010), (001), (110), (011), (101), and (111)], the fine-tuning of the desired morphologies can be achieved by controlling the values of the surface energies, thereby lending a microscopic understanding to the experimental results. The as-synthesized α-AgVO₃ crystals display a high antibacterial activity against methicillin-resistant *Staphylococcus aureus*. The results obtained from the experimental and theoretical techniques allow us to propose a mechanism for understanding the relationship between the morphological changes and antimicrobial performance of α-AgVO₃.

KEYWORDS: α-AgVO₃, morphologies, first-principles calculations, photoluminescence, Wulff construction, antibacterial activity

1. INTRODUCTION

AgVO₃ is the most commonly occurring structure of silver vanadium oxide-based materials in the solid state.[1] Four polymorphs, the metastable α-, γ-, and δ-forms and the more stable β-type, have been described.[2,3] Fleury and Kohlmuller[4] presented X-ray diffraction (XRD) results without structural analysis. Thenceforth, structural chemistry studies of these phases were developed.[2,3,5−7] β-AgVO₃ is the more stable polymorph and presents a monoclinic space group (I2/m No. 12),[6] while α-AgVO₃ is a metastable phase of the monoclinic C2/c (No. 15) system. α-AgVO₃ is irreversibly transformed to β-AgVO₃ at 200 °C.[2] Consequently, polymorphism is a property inherent to AgVO₃.

Metastable compounds offer tremendous opportunities to obtain new materials with unusual properties that drive the efforts to understand and optimize their synthesis and stabilization. From the viewpoint of flourishing scientific interest and technological applications, the study of AgVO₃ polymorphic materials provides an exciting platform for investigation owing to their versatile properties resulting from the diverse phase transitions of AgVO₃. Our research group is

involved in a project devoted to studying complex metal oxides, such as α-Ag₂WO₄, as efficient microbial agents.[8] In addition, the synthesis and characterization of metastable phases such as β-Ag₂WO₄[9,10] and γ-Ag₂WO₄[11,12] and, in a very recent paper, the synthesis and characterization of the stable phase of β-AgVO₃[13] have also been reported. Working closely with experimentalists on the comprehension of the surface properties of complex multifunctional materials requires the use and development of several computational strategies where a precise knowledge of their optimal geometry and structure is a mandatory prerequisite to computational modeling. Theoretical simulations can address several properties of the materials: the morphology, the surface structure below genuine thermodynamic environments, and analytical descriptors of antibacterial activity. With the information provided by the theoretical results, a plethora of experimental data can be better matched to computer simulations, providing synergy between

different experimental techniques and theory. This work is a continuation of these earlier studies, in which a combination of theory and experiments is performed, and our motivation is principally fueled by discovering a novel synthesis of metastable phases with novel properties.

Previous works on the synthesis of metastable α-AgVO$_3$ have either reported the requirements of high temperatures or long reaction times or showed poor crystalline structures or low purity.[2,14,15] Later, Shao and co-workers[16] successfully synthesized pure α-AgVO$_3$ with a high crystallinity through a biomimetic process. Very recently, McNulty et al.[17] described the achievement of α-AgVO$_3$ nanowires via a hydrothermal treatment and the structural transformation of α-AgVO$_3$ to the tunnel-structured β-AgVO$_3$ by annealing at 475 °C.

Here, we synthesized α-AgVO$_3$ samples by using the coprecipitation (CP) method at low temperatures. The characterizations of the structures, morphologies, and optical properties were performed by experimental techniques such as X-ray diffraction (XRD) with Rietveld analysis, Raman (MR) spectroscopy, field-emission scanning electron microscopy (FE-SEM), ultraviolet−visible (UV−vis) diffuse reflectance spectroscopy, and photoluminescence (PL). Later, we focus on the analysis of the antibacterial activity against methicillin-resistant *Staphylococcus aureus* (MRSA), by determining the minimum inhibitory/bactericidal concentrations (MIC/MBC). First-principles quantum-mechanical density functional theory (DFT) calculations are used to supplement these experimental techniques.

2. EXPERIMENTAL PROCEDURES

2.1. Synthesis. The α-AgVO$_3$ were acquired by CP method. For this are used silver nitrate (AgNO$_3$, 99% purity, Synth) and ammonium monovanadate (NH$_4$VO$_3$, 99% purity, Sigma-Aldrich). Initially, 1 mmol of NH$_4$VO$_3$ and 1 mmol of AgNO$_3$ were individually melted in 35 mL of water, under agitation, at 30 °C. The solutions were jumbled, and a quick materialization of solid α-AgVO$_3$ (yellow coloration) occurred. The CP was performed at 10, 20, and 30 °C. The powders was washed with distilled water and dried in an oven at 60 °C for 12 h.

2.2. Characterization. The α-AgVO$_3$ powders were characterized by X-ray diffraction using a Rigaku-DMax/2500PC with Cu Kα radiation (λ = 1.5406 Å) in the 2θ range from 10° to 80° with a scanning speed of 0.02°/min. The Rietveld refinements were done by using the general structure analysis (GSAS) program using with XDR patterns in the 2θ range from 10° to 110° with a scanning rate of 0.01°/min. Raman spectroscopy was done in a spectrometer (Horiba Jobin-Yvon) coupled to a CCD Synapse detector and an argon ion laser, operating at 532 nm with maximum power of 1.2 mW. The spectra were measured in the range from 5 to 1000 cm^{-1}. UV−vis spectra were collected with a Varian spectrophotometer model Cary 5G in diffuse reflection mode. The morphologies were investigated by field emission scanning electron microscopy (FE-SEM) with a Supra 35-VP Carl Zeiss instrument operated at 15 kV. In addition, transmission electron microscopy (TEM) analyses operating at 200 kV and energy dispersive X-ray spectroscopy (EDS) were performed with a FEI microscope model Tecnai G2 F20. The PL measurements were performed with a Monospec 27 monochromator (Thermal Jarrel Ash) coupled to a R446 photomultiplier (Hamamatsu Photonics). A krypton ion laser (Coherent Innova 90 K) (λ = 350 nm) was used as excitation source, keeping its maximum output power at 500 mW. All experiments measurements were performed at room temperature.

2.3. Theoretical Methods. First-principles total-energy calculations were performed using the DFT framework as implemented in the VASP package.[18] The generalized gradient approximation in the Perdew−Burke−Ernzerhof formulation for electron exchange and correlation contributions to the total energy were used to solve the Kohn−Sham equations.[19,20] The relaxed systems were generated by means of the conjugated gradient energy minimization scheme when the Hellmann−Feynman forces converged to less than 0.01 eV/Å per atom. Projector augmented wave pseudopotentials were used to describe the electron−ion interaction. A cutoff energy of 520 eV was selected to truncate the plane-wave expansion, and the Brillouin zones have been sampled through Monkhorst−Pack special k-points grids that ensure geometrical and energetic convergence for the α-AgVO$_3$ structures. Vibrational frequency calculations were performed at the Γ-point, and the dynamical matrix was computed by numerical evaluation of the first derivative of the analytical atomic gradients.

Stoichiometric slabs for low Miller index surfaces of monoclinic α-AgVO$_3$ structure were modeled, and the surface energy values, E_{surf}, were calculated. After the corresponding optimization process and convergence tests in thickness, slab models consisting of eight molecular units were obtained for (100), (010), (001), (110), (011), (101), and (111) surfaces, with areas of 56.1, 58.2, 53.5, 40.4, 121.7, 129.4, and 71.0 Å, respectively. The equilibrium shape of a crystal is calculated by the classic Wulff construction, which minimizes the total surface energy E_{surf} at a fixed volume, providing a simple relationship between the E_{surf} of the plane (hkl) and its distance in the normal direction from the center of the crystallite.[21] Therefore, the crystallite shape of several materials can be determined.[22−26]

2.4. Antibacterial Effect of the α-AgVO$_3$ Synthesized at Different Temperatures. In this work, the as-synthesized α-AgVO$_3$ microcrystals were also investigated for their antibacterial effect against MRSA by determining the minimum inhibitory/bactericidal concentrations (MIC/MBC) to planktonic cells of one reference strain from the American Type Culture Collection (MRSA ATCC 33591).

The antibacterial tests were carried out according to the Clinical and Laboratory Standards Institute (CLSI) broth microdilution method (document M7-A7, 2006 for the bacteria).[27] The standard strain of MRSA was inserted onto Mueller Hinton agar plates (Acumedia Manufactures Inc., Baltimore, MD) and kept in a greenhouse at 37 °C for 24−48 h. After the incubation, 10 colonies of the fresh cells of the microorganism grown on the agar plates were transferred to tryptic soy broth (TSB) (Acumedia Manufactures, Inc. Baltimore, MD) and incubated during 12 h in an orbital shaker at 37 °C (75 rpm). The cells were washed two times with phosphate-buffered saline (PBS) solution at pH 7.2, and centrifuged at 5000g for 5 min. Bacteria cells were resuspended in TSB and the MRSA suspension was spectrophotometrically standardized to a final concentration of 10^7 cfu/mL determined by optical density measurements of the suspension. Then, the adjusted inoculum suspension was diluted in broth culture medium, and after inoculation with microcrystals, each well contains approximately 10^5 cfu/mL.

To determine the MICs and MBCs, MRSA was exposed to 2-fold serial dilutions of each of the α-AgVO$_3$ solutions (from 1000 to 0.061 μg/mL) in TSB culture medium in 96-well microtiter plates, and the plates were incubated for 24 h at 37 °C. Positive controls were inoculated culture medium without the α-AgVO$_3$ microcrystals, while uninoculated culture medium was used as negative controls. The MIC was defined as the lowest concentration of each microcrystal that inhibits microbial growth by visual inspection.[27−29] MBCs values were determined by calculating colony forming units (cfu/mL) of the diluted aliquots from 10-fold serial dilutions (10^{-1}−10^{-8}) of each well, which were inoculated (25 μL) on Mueller Hinton Agar twice. After 24−48 h of incubation at 37 °C, the colony forming units per mililiter were calculated and log$_{10}$-transformed. The MBCs values were the lowest concentration of each of the α-AgVO$_3$ solutions resulting in no bacterial growth.[28,29]

3. RESULTS

3.1. Ordering at Long-Range: X-ray Diffraction. The XRD patterns of α-AgVO$_3$ obtained by CP at different temperatures are presented in Figure 1a. The samples prepared at 10, 20, and 30 °C have analogous peaks, which were attributed to the monoclinic phase α-AgVO$_3$, with space group $C2/c$ (No. 15), in agreement with the Inorganic Crystal
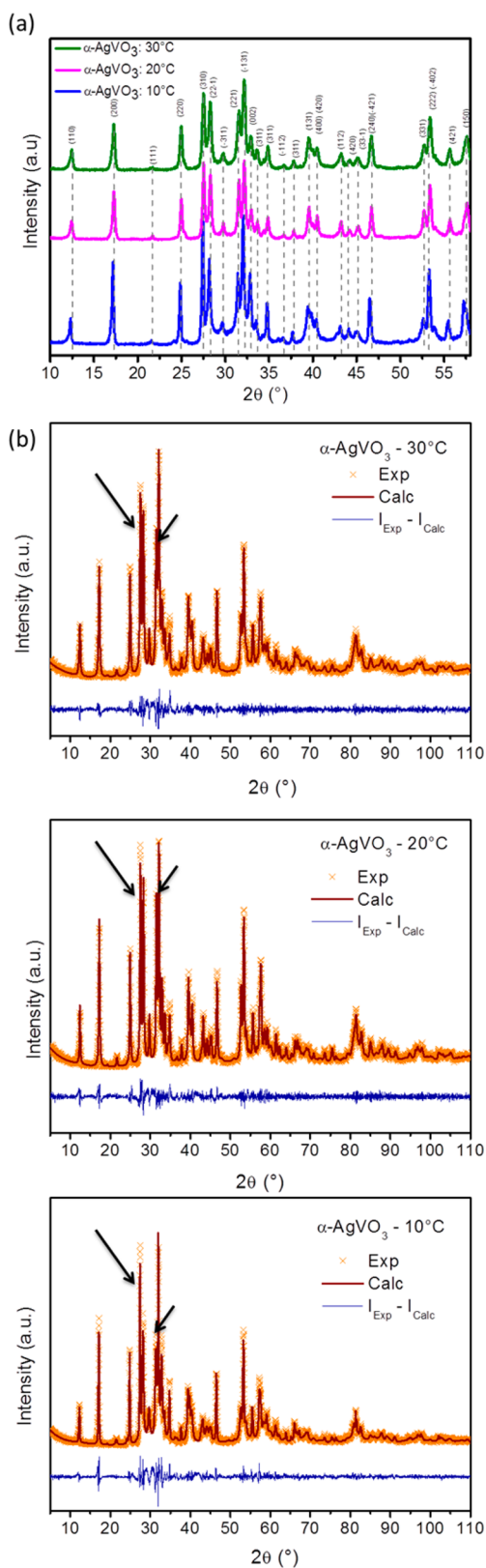
Figure 1. (a) XRD patterns of α-AgVO₃ synthesized by the CP method at 10, 20, and 30 °C. (b) Rietveld refinement of α-AgVO₃.

Structure Database pattern no. 50645. This indicated a high phase purity in the three samples. The low resolution of the peaks indicates that none of the α-AgVO₃ powders obtained by

the CP method were totally crystallized and therefore present structural disorder at long range.

Figure 1b shows the Rietveld refinement graphics of the α-AgVO₃ powders synthesized by the CP method at 10, 20, and 30 °C. The Rietveld refinement[30] analysis results are displayed in Table 1, and the parameters (R_{Bragg}, R_p, R_{wp}, and χ^2) indicate a high agreement among the XRD patterns, calculated and observed, for the α-AgVO₃ phase obtained at 10, 20, and 30 °C. Moreover, the lattice parameters (a, b, c) and bond angle (β) estimated from the refinement confirm the monoclinic structure of this material and are in concordance with the literature.[2] However, with increasing temperature, an expansion of the cell volume was observed and can be linked with the rise in lattice parameter a (see Table 1).

An analysis of the refinement graphs (see Figure 1b) indicates that a change in the intensities of the two main peaks corresponding to the (310) and (22$\bar{1}$) directions (located at 27.53 and 28.25°, respectively) is observed. For the α-AgVO₃ phase obtained at 10 °C, a large difference in the intensity between the two peaks is observed; however, for the powders obtained at 20 and 30 °C, this difference is not so significant. This result may indicate a preferential growth owing to a symmetry-breaking process that causes distortions/deformations in the [AgO₆] and [VO₄] clusters.

The geometric optimizations of the α-AgVO₃ crystal structure and a 3D polyhedral representation of the optimized structure are displayed in Figure 2a. The α-AgVO₃ phase belongs to the C2/c space group, and the calculated unit cell parameters are a = 10.6192 Å, b = 10.0698 Å, c = 5.5738 Å, and β = 100.41°. Geometrical parameters of the adjusted structure are in agreement with the literature.[2] An analysis of the results indicates that the silver atoms are coordinated with six oxygen atoms to form octahedral [AgO₆] clusters, while four oxygen atoms are coordinated with a vanadium atom, forming tetragonal [VO₄] clusters. There are two types of octahedral [AgO₆] units with highly distorted geometries, resulting in two types of O–Ag–O bond angles (Figure 2b).

To understand the influence of the synthesis temperature on the distortions within the lattice of the clusters, the bond distances and angles for the α-AgVO₃ patterns of samples synthesized at 10, 20, and 30 °C were obtained. In addition, the theoretical values obtained by DFT calculations are also reported in Figure 2. An analysis of the results depicted in Figure 2b reveals that the temperature promotes a disordering at long range for this material, owing to distortions/deformations in the Ag–O and/or V–O bonds and in the O–Ag–O and/or O–V–O bond angles. The α-AgVO₃ pattern for the sample synthesized at 10 °C has a greater degree of disorder in the bond angles when compared to the others; hence, it can be affirmed that the increase in the synthesis temperature improves the system organization.

3.2. Ordering at Short Range: Raman Spectroscopy. Consistent with the group theory analysis, the allowed representation for the corresponding Wyckoff positions of the α-AgVO₃ structure in the C2/c space group points out 30 Raman active modes corresponding to the decomposition at the Γ point ($\Gamma = 14A_g + 16B_g$).

Figure 3a shows the experimental Raman spectra of the α-AgVO₃ powders obtained at 10, 20, and 30 °C, which agree with the literature.[15,31] Eighteen Raman-active modes are observed. The strongest band at 919 cm⁻¹ may originate from symmetric stretching that bridges either V–O–Ag or O–V–O vibrations. The band at 896 cm⁻¹ can be linked with the

Table 1. Rietveld Refinements Result of α-AgVO₃ Powders[a]

ST (°C)	lattice parameter (Å)			β (deg)	CV (Å³)	R_{Bragg} (%)	χ^2 (%)	W_{Rp} (%)	R_p (%)
	a	b	c						
10	10.4355	9.9221	5.5171	99.539	563.358	0.0695	2.746	0.1115	0.0879
20	10.4476	9.9136	5.5221	99.616	563.911	0.0878	1.734	0.0939	0.0718
30	10.4561	9.9245	5.5223	99.588	565.067	0.0629	1.853	0.0892	0.0700
ref 2	10.437(2)	9.897(2)	5.532(4)	99.69(4)	563.280				

[a]ST = synthesis temperature. CV = cell volume.
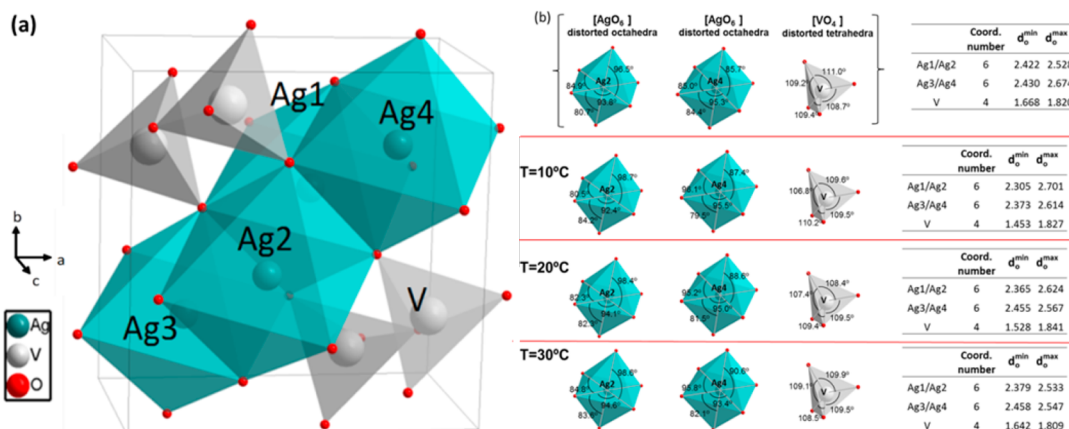
Figure 2. (a) α-AgVO₃ bulk structure represented by the constituent polyhedra, in the primitive unit cell. (b) Geometry of the different clusters determined by DFT calculations and for the α-AgVO₃ structure synthesized at 10, 20, and 30 °C.
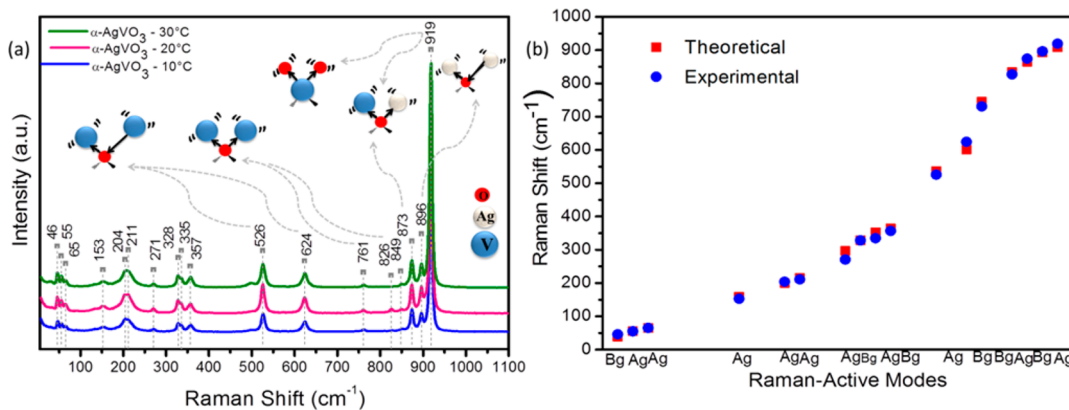
Figure 3. (a) Raman spectra of α-AgVO₃ sample. (b) Comparison between experimental and theoretical Raman spectra of α-AgVO₃.

stretching vibrations of Ag−O−Ag bridges, while the bands at 886 and 873 cm⁻¹ can be connected to stretching vibrations of the V−O−Ag bridges. The presence of a V−O−V is associated with the bands appearing at 849, 826, 761, 730, 624, and 526 cm⁻¹, related to the asymmetric and symmetric stretching modes.[15,31−33]

For a better observation of the Raman modes, a close-up between 10 and 270 cm⁻¹ was performed [Figure S1 in the Supporting Information (SI)]. It can be observed that the modes are not well-defined and that there is a slight difference in the definition of the peaks for the α-AgVO₃ powders obtained at 10, 20, and 30 °C. This phenomenon can be associated with different levels of distortions in the [AgO₆] and [VO₄] clusters at short range. Again, it is possible to observe that the powder synthesized at 10 °C presents a lower grade of ordering and that the organization increases with the synthesis temperature, as the definition of the peaks is improving.

In Figure 3b and Table S1 (in the SI), the experimental and calculated Raman-active modes are compared with the literature results. An examination indicates that both results are in concordance, but a little difference is noted between literature and our results.

3.3. Ordering at Medium Range: UV−Vis Spectra and PL Measurements. *3.3.1. UV−Vis Absorption Spectra.* Figure 4 shows the linear dependence of the absorbance of the α-AgVO₃ obtained from a modified Kubelka−Munk[34] and Wood−Tauc[35] function, F(R), on the photon energy (hν). The band gap values of the α-AgVO₃ samples synthesized at 10, 20, and 30 °C are 2.45, 2.35, and 2.40 eV, respectively, which is in accordance with the literature.[36]

A slope can be observed in the optical absorption curves for all samples, which decreases the band gap value of these materials. According to Figure 4a, if the material was ordered, a well-defined absorption would be observed, and thus, a band gap value of about 2.8 eV was expected (as can be seen in
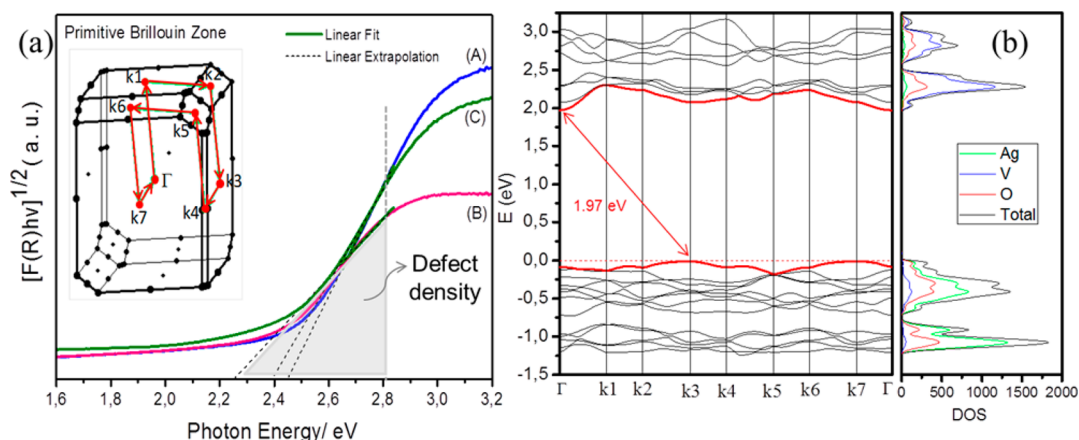
Figure 4. (a) UV−vis diffuse reflectance of α-AgVO₃ synthesized by the CP method at 10 °C (A, 2.45 eV), 20 °C (B, 2.25 eV), and 30 °C (C, 2.40 eV). (b) Calculated band structure and DOS projected on atoms for α-AgVO₃ [k1 (001), k2 (101), k3 (100), k4 (110), k5 (111), k6 (011), and k7 (010)].

Figure 4a); however, the density of defects present in the material causes a reduction in the band gap. Therefore, these tails indicate that there are localized electronic levels within the forbidden band associated with the presence of bond distortions that cause a lattice structural disorder, as previously observed in the XRD patterns and Raman measurements. Therefore, we can conclude that the α-AgVO₃ samples synthesized at 10, 20, and 30 °C are disordered at medium range.

An indirect band gap (from k3 to Γ) of 1.97 eV and a direct band gap of 2.05 eV were obtained from the calculated band structure of α-AgVO₃, which are a little lower than the experimental values, but it is well-known that the Perdew−Burke−Ernzerhof functional underestimates the band gap values. The Brillouin zone with the path used, the band structure, and the density of states (DOS) projected on the atoms are presented in Figure 4a,b. The DOS analysis points out that the upper part of the valence band consists of noninteracting Ag-4d and O-2p orbitals, and a high contribution of V-3d and Ag-5s orbitals is perceived in the lower part of the conduction band.

3.3.2. PL Measurements. The PL spectra are presented in Figure 5 for the α-AgVO₃ obtained by the CP method at 10, 20, and 30 °C. For all samples a broad band profile is shown in the PL spectra, which covers a region from 350 to 850 nm and is
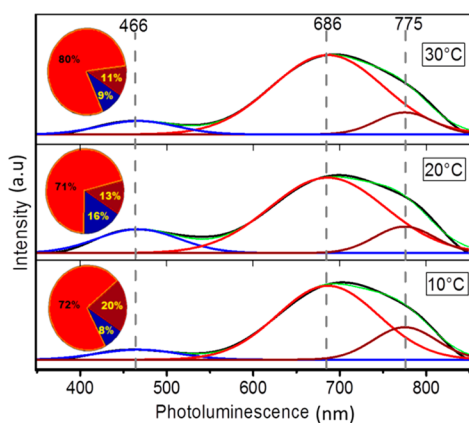

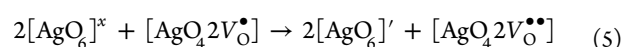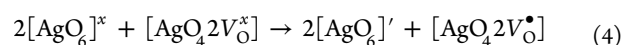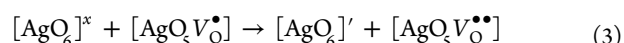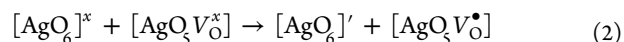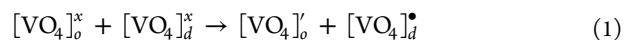**Figure 5.** PL spectra and deconvolution for α-AgVO₃ synthesized at 10, 20, and 30 °C.

centered at around 466 nm in the blue region and 686 nm in the red region. This comportment is linked to multiphonon or multilevel routes that involve the contribution of many energy states inside the band gap.[37] The vacancies, distortions, and symmetry breaking between clusters are creating energy states within the band gap and, thus, generate the PL properties.
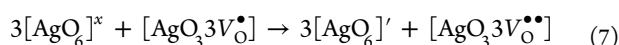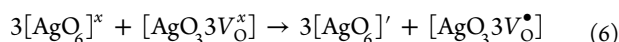
The α-AgVO₃ semiconductor is formed by interconnected ([VO₄]−[AgO₆]−[VO₄]−[AgO₆]...) clusters (see Figure 2b). Distortions and symmetry-breaking processes in the tetrahedral [VO₄] and octahedral [AgO₆] clusters, defined as shallow holes, are mainly responsible for the blue PL emission, while the red PL emission is mainly caused by oxygen vacancies, defined as deep holes.[37−39]

To understand the PL properties and their dependence on the structural order−disorder of the lattice, a deconvolution of the PL emission is made (Figure 5). Three peaks are added (area Voigt function) and fixed at positions: blue (maximum below 466 nm), red (maximum below 686 nm), and infrared regions (maximum below 775 nm.

It can be seen that the spectrum of the α-AgVO₃ is mainly dominated by emission in the red region (deep holes); 90% of the PL emission is in this area, while only about 10% of the emission is in the blue region (shallow holes). So, the shallow holes present a lower contribution for the PL spectrum. Therefore, the origin of PL emission in α-AgVO₃ powders is mainly due to O vacancies ($V_O^{\bullet}$, $V_O^{\bullet\bullet}$, and V_O^{x}), and these complex defects are deeply introduced in the band gap.

In our wide-band model, the PL properties of the semiconductors can be explained using the Kröger−Vink notation.[40] In this model, the PL response of solids is influenced by middle energy states inside the band gap. After the photon absorption, the recombination of electrons/holes includes the cluster-to-cluster charge allocation process, which can be elucidated by the eqs 1−7)

$$[VO_4]_o^x + [VO_4]_d^x \rightarrow [VO_4]_o' + [VO_4]_d^{\bullet} \tag{1}$$

$$[AgO_6]^x + [AgO_5 V_O^x] \rightarrow [AgO_6]' + [AgO_5 V_O^{\bullet}] \tag{2}$$

$$[AgO_6]^x + [AgO_5 V_O^{\bullet}] \rightarrow [AgO_6]' + [AgO_5 V_O^{\bullet\bullet}] \tag{3}$$

$$2[AgO_6]^x + [AgO_4 2V_O^x] \rightarrow 2[AgO_6]' + [AgO_4 2V_O^{\bullet}] \tag{4}$$

$$2[AgO_6]^x + [AgO_4 2V_O^{\bullet}] \rightarrow 2[AgO_6]' + [AgO_4 2V_O^{\bullet\bullet}] \tag{5}$$

$$3[AgO_6]^x + [AgO_3 3V_O^x] \rightarrow 3[AgO_6]' + [AgO_3 3V_O^\bullet] \quad (6)$$

$$3[AgO_6]^x + [AgO_3 3V_O^\bullet] \rightarrow 3[AgO_6]' + [AgO_3 3V_O^{\bullet\bullet}] \quad (7)$$

where $[VO_4]_o^x$, $[AgO_6]^x$, $[AgO_5 V_O^x]$, $[AgO_4 2V_O^x]$, $[AgO_3 3V_O^x]$, $[VO_4]'$, and $[AgO_6]'$ are electron donors; $[AgO_5 V_O^\bullet]$, $[AgO_4 2V_O^\bullet]$, and $[AgO_3 3V_O^\bullet]$ are electron donors/acceptors; and $[VO_4]_d^\bullet$, $[AgO_5 V_O^{\bullet\bullet}]$, $[AgO_4 2V_O^{\bullet\bullet}]$, and $[AgO_3 3V_O^{\bullet\bullet}]$ are electron acceptors.

3.4. Morphological Aspects. The morphologies of the self-assembled structures of α-AgVO$_3$ were investigated in detail. The images of the α-AgVO$_3$ samples obtained at 10, 20, and 30 °C are depicted in Figure 6.
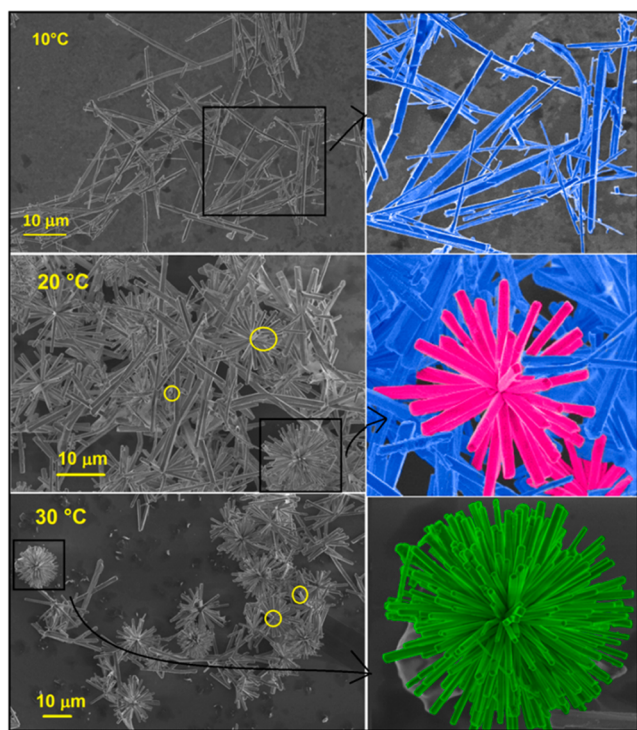
Figure 6. FE-SEM imagens of α-AgVO$_3$ powders obtained by the CP method at 10, 20, and 30 °C.

Crystallization of α-AgVO$_3$ is influenced by the solvent (H$_2$O), precursors (NH$_4^+$ and NO$_3^-$), and temperature involved in the reaction. The initial clusters formed in the solution [VO$_3^-$ aq and Ag(NH$_3$)$^{2+}$ aq] are the building blocks for the early stages of the nucleation process; these, in turn, may create nano- or microparticles (amorphous, crystalline, and semicrystalline). Water, NO$_3^-$, and NH$_4^+$ are important in the formation, nucleation, and growth of α-AgVO$_3$. These organizations based on symmetry can take place at three levels: short, medium, and long distances. Thus, the clusters can interact preferably, forming surfaces that can give rise to numerous morphologies (Figure 6). Because of the clusters, defects, and electronic density, complex clusters were formed with nonzero dipole moments. The dipole−dipole interactions may generate clusters with a defined number of atoms to favor growth in a particular direction. Thus, in complex clusters, there is a correlation among the electrons situated in the neighborhood of the [AgO$_6$] and [VO$_4$] complex clusters, provided by long-range interactions. These interactions harmonize the interactions at short and medium ranges,

starting with the charge transfer and separation. At medium range, there are correlations among the rotational motion of stable moments in dissimilar [AgO$_6$]−[AgO$_6$], [AgO$_6$]−[VO$_4$], and [VO$_4$]−[VO$_4$] complex clusters, and at short range, there are polarization processes of [AgO$_6$] or [VO$_4$] clusters because of the permanent moment of other neighboring clusters.[41,42] These complex clusters are loaded with a positive or negative charge, inducing a more effective action to the Brownian effect influenced by the temperature, which increases the number of collisions between the complex clusters formed. Thus, synthesis at different temperatures leads to the formation of wires, rods, or urchinlike microspheres[41−43] according to the proposed mechanisms in Figure 7.
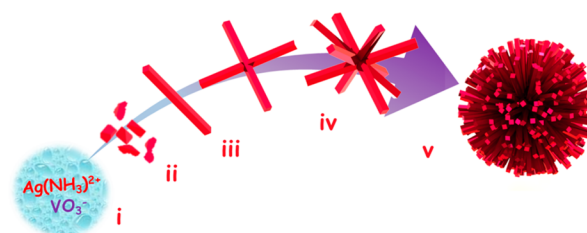

Figure 7. Illustration of the formation process of the urchinlike α-AgVO$_3$ microspheres: (i) formation of initial clusters in the solution, (ii) formation of nano- or microparticles (amorphous, crystalline, and semicrystalline), (iii) the bulk materials split into α-AgVO$_3$ nanorods, (iv) self-assembly of α-AgVO$_3$ nanorods, and (v) formation of α-AgVO$_3$ urchinlike microspheres.

Figure 6 indicates the formation of a large quantity of microrod α-AgVO$_3$ crystals in the synthesis performed at 10 °C. These crystals have defined faces and are elongated along the y-axis in the [110] direction. The diameter of the microrods is uniform throughout their lengths. At 20 °C, it can be seen that the microrods begin to agglomerate, and some urchin-like microspheres are formed by the direct self-assembly of nanorods due to molecular interactions. At 30 °C, α-AgVO$_3$ crystals with urchinlike morphologies are predominantly formed.

The Wulff crystal illustration of adjusted α-AgVO$_3$ and the diverse morphologies that would be found by adjustment of different surface energy proportions for numerous facets are presented in Figure S2 of the SI. Transformations between the different morphologies are associated with geometric constraints enforced by the crystal structure and are linked with the relative surface energy values of every surface. This interpretation has the benefit that all faces grow from the original α-AgVO$_3$ crystal (ideal) dependent on the surface energy value. Figure 8 illustrates the tetragonal rodlike shape extended alongside the x- and y-axes in the [110] direction, and in this case, the crystals exhibit six faces. A good relation among experimental and theoretical morphologies is observed: (i) when the surface energy of the (001) orientation declined to 0.24 J/m^2 and that of (110) decreased to 0.16 J/m^2 and (ii) when the surface energy of the (011) orientation is reduced to 0.12 J/m^2.

As noted in previous analysis, the predominant morphologies obtained experimentally (Figure 8) display exposed (001), (011), and (110) surfaces, which supports the hypothesis that these surfaces are stabilized by interactions with water molecules in the solvent. These results indicated that the
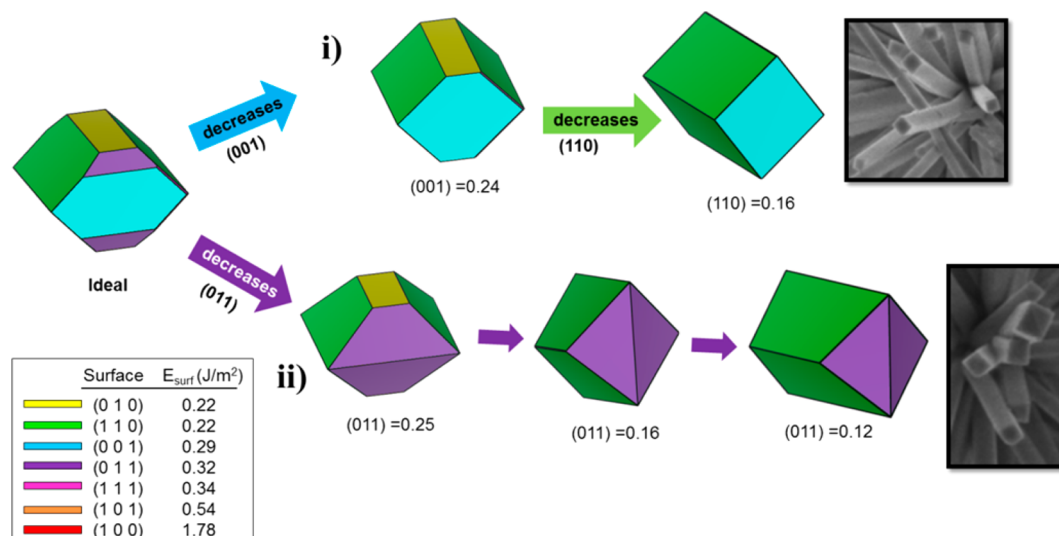
Figure 8. Tetragonal rodlike crystals exhibiting six faces with different crystallographic planes: (i) (001), (001), (110), (110), (110), and (110), with elongation of the *x*- and *y*-axis along the [110] direction, and (ii) (011), (011), (011), (011), (110), (110), (110), (110), with elongation in the [110] direction.
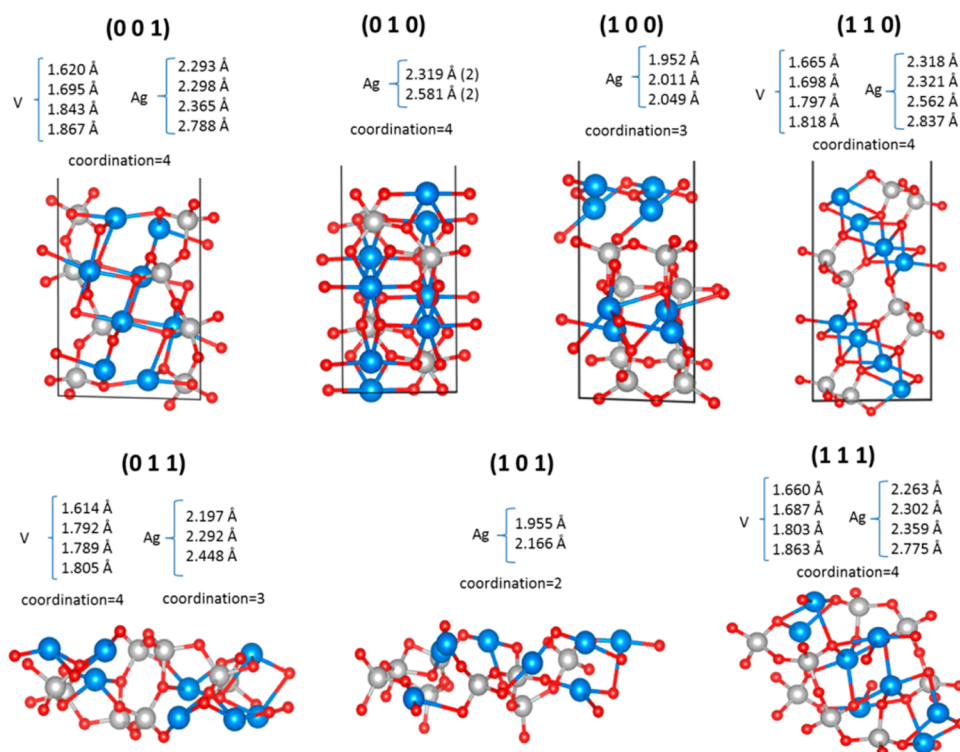

Figure 9. Schematic representations of surfaces of α-AgVO$_3$. The Ag–O and V–O bond distances of the exposed V and Ag atoms are shown.

Wulff shape of α-AgVO$_3$ is narrowly associated with the chemical environs.

The low-index (001), (010), (100), (110), (011), (101), and (111) surfaces of α-AgVO$_3$ are presented in Figure 9. The (010), (100), and (101) surfaces are oxygen- and silver-ended, while the (001), (110), (011), and (111) surfaces are vanadium−oxygen- and silver-ended. Because of the atomic conformation of the uncovered facets, the synthesis temperature has a significant influence on the reactivity and equilibrium of the faces. On the (001), (010), (110), and (111) surfaces, silver atoms are coordinated with four oxygen atoms to obtain $[AgO_42V_O^x]$ complex clusters. The (100) and

(011) surfaces have silver atoms bordered by three oxygen atoms, resulting in the $[AgO_33V_O^x]$ complex clusters, while for the (101) surfaces, silver atoms are only coordinated with two oxygen atoms, forming $[AgO_24V_O^x]$ complex clusters (disfavoring its stability). The bond distances for the exposed clusters in each surface are shown in Figure 9.

3.5. Measurements of the Antibacterial Activities of the α-AgVO$_3$ Synthesized at Different Temperatures. The antibacterial activities of α-AgVO$_3$ synthesized at different temperatures were studied against the Gram-positive bacteria, methicillin-resistant *S. aureus*, and the results of this study, i.e., the MIC and MBC tests, are presented in Figure 10. The
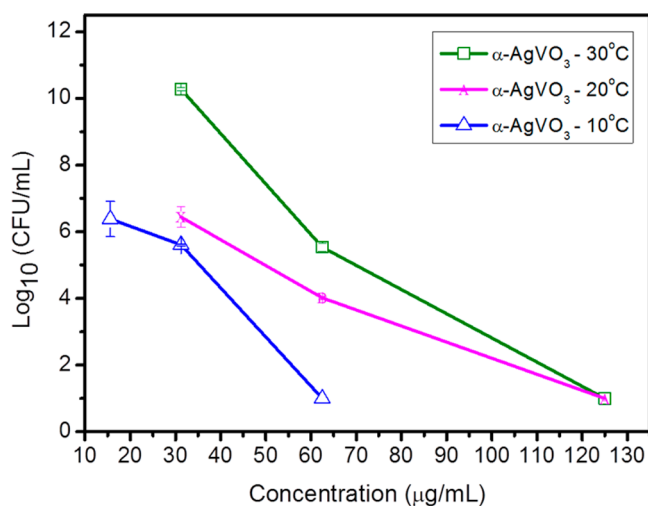
Figure 10. Summary of $\log_{10}$ cfu/mL values of MRSA obtained for the subinhibitory concentrations of the α-AgVO$_3$ microcrystals synthesized by the CP method at 10, 20, and 30 °C. Control = 11.48 $\log_{10}$ cfu/mL (± 0.5).

results demonstrate that, regardless of the time used in the synthesis, the α-AgVO$_3$ microcrystals had both bacteriostatic and bactericidal activity against MRSA. In addition, for each sample, the concentration that caused no visible growth (MIC value) also prohibited colonies on the plates after incubation (MBC value). But, when microcrystals synthesized at 10 °C were used, the MIC/MBC value was lower (62.5 μg/mL) than those observed for the samples synthesized at 20 and 30 °C, which were similar (approximately 125 μg/mL) to one another (Figure 10). Even at concentrations inferior than the MIC/MBC standards, the α-AgVO$_3$ microcrystals were still able to diminish bacterial growth. When MRSA was incubated deprived of α-AgVO$_3$ microcrystals (control), a count of 11.48 $\log_{10}$ cfu/mL was obtained. Figure 11 shows the representative photographs of MRSA growth when exposed to α-AgVO$_3$ (synthesized at 10 °C) at various concentrations: (a) inhibitory concentration (MBC concentration), (b) intermediate concentration (MIC), and (c) control group (not exposed to α-AgVO$_3$).

The mechanism of the antibacterial activity of a semiconductor is ascribed to the oxidative stress provoked by the production of OH*, O$_2$′, and O$_2$H* (reactive species).[44,45] These reactive species are formed when $[VO_4]_d^\bullet$, $[AgO_5V_O^\bullet]$, $[AgO_4 2V_O^\bullet]$, $[AgO_3 V_O^\bullet]$, $[AgO_5 V_O^{\bullet\bullet}]$, $[AgO_4 2V_O^{\bullet\bullet}]$, and $[AgO_3 3V_O^{\bullet\bullet}]$ complex clusters transfer a hole for water that decomposes into hydroxyl radicals and protons (OH* and H$^\bullet$).

Simultaneously, $[AgO_5V_O^\bullet]$, $[AgO_4 2V_O^\bullet]$, $[AgO_3 3V_O^\bullet]$, $[VO_4]_o'$, and $[AgO_6]'$ can transfer an electron to the oxygen molecule (O$_2$) and produce O$_2$′, which interacts with the proton, forming an O$_2$H* radical.

On the basis of previous literature, we proposed that a plausible mechanism of α-AgVO$_3$ inactivation of MRSA bacteria implicates the collaboration among specific (001) and (011) surfaces. According to the Wulff crystal representation of optimized α-AgVO$_3$ presented in Figures 8 and S2 of the SI, these faces present low surface energies ($E_{surf} = 0.24$ and 0.12 J/m^2, respectively) as determined by ab initio calculations; therefore, they are more easily polarized and able to generate OH*, O$_2$′, and O$_2$H*, which are responsible for cell death.

The α-AgVO$_3$ nanorods synthesized at 10 °C have an antibacterial efficiency higher than other microcrystals. Thus, we can state that an efficient antibacterial activity is affected by the morphologies of the particle, since the formation of α-AgVO$_3$ with an urchinlike morphology at 20 and 30 °C decreases the amount of the reactive surface and, consequently, the efficient antibacterial activity of the material.

The above results show the importance of the formation of defects (in particular, on the semiconductor surface), and the elimination of these surfaces by the formation of agglomerates results in a lower bactericidal efficiency. Additionally, the (001) and (011) surfaces present Ag atoms with incompletely coordinated atoms, according to the slab model shown in Figure 9. Usually, the surfaces with dangling bonds have a higher reactivity.[46]

In addition, it was observed by XRD/Rietveld refinement and Raman, UV–vis, and PL measurements that the α-AgVO$_3$ synthesized at 10 °C presents a greater degree of distortions at short, medium, and long ranges than the α-AgVO$_3$ synthesized at 20 and 30 °C. These distortions of the bond angles cause a difference in the electron densities in the [VO$_4$] and [AgO$_6$] clusters, and therefore, an electronic polarization of the clusters; they also stabilize the charge separation (electron–hole) and make the material more reactive and, hence, more efficient for cell death, as illustrated in Figure 12.

4. CONCLUSIONS

The flexibility in materials design afforded by metastable materials opens up opportunities for exciting new device areas that drive efforts to understand and optimize their synthesis and stabilization. In the current study, for the first time, the optical properties and the morphological evolution of the α-AgVO$_3$ metastable phase were systematically investigated and correlated with the antibacterial activity of this material by joining experimental methods and first-principles calculations.
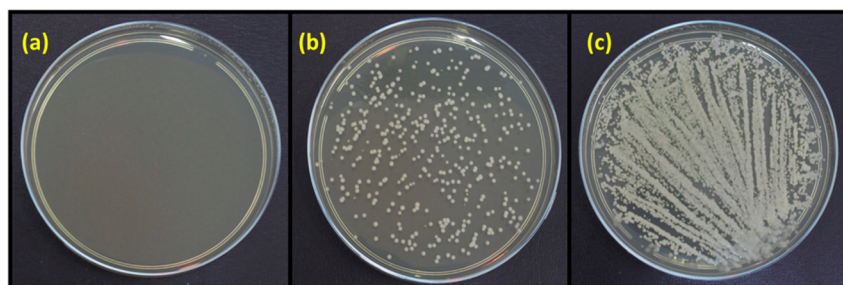

Figure 11. Representative photographs of *Staphylococcus* exposed to α-AgVO$_3$ at the (a) MBC concentration and (b) subinhibitory concentration (MIC). (c) *Staphylococcus* incubated without α-AgVO$_3$ microcrystals (control).
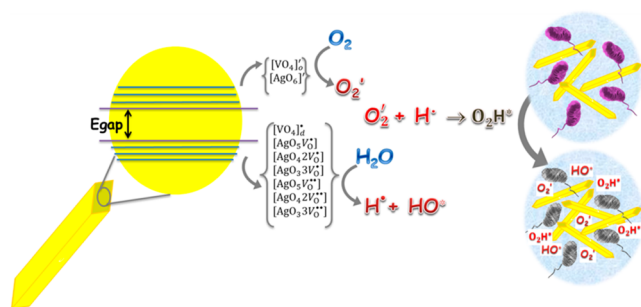
Figure 12. Proposed reaction mechanism of the antibacterial activity of the semiconductor α-AgVO$_3$.

The powders were synthesized by the CP method at 10, 20, and 30 °C. The XRD patterns and Rietveld refinement data show that these samples are monophasic with a monoclinic structure.

The geometric optimization of the crystal structure indicates that α-AgVO$_3$ is composed of octahedral [AgO$_6$] and tetragonal [VO$_4$] distorted clusters. These distortions are observed at long, short, and medium ranges by XRD, Raman spectroscopy, and UV–vis diffuse reflectance, respectively. PL measurements demonstrate that the α-AgVO$_3$ obtained at different temperatures has intermediate electronic levels inside the band gap. The morphologies of α-AgVO$_3$ are optimized by Wulff crystal construction. By presumptuous diverse surface energy proportions for some facets, a good arrangement among experimental and theoretical morphologies is established.

The as-synthesized α-AgVO$_3$ crystals display a high antibacterial activity against MRSA. The results obtained from the experimental methods and first-principles calculations allow us to propose a mechanism devoted to understanding the relationship between structural order−disorder effects, morphological aspects, and the antimicrobial performance of α-AgVO$_3$. The biological tests showed that the α-AgVO$_3$ crystals with rodlike morphologies and predominant (011) and (001) surfaces with small surface energies had greater antibacterial activity for the inactivation of MRSA bacteria. The main conclusion of this work is that different morphologies of α-AgVO$_3$ crystals display noticeably dissimilar chemical and physical properties and that information on their electronic properties permits one to progress their applications.

ASSOCIATED CONTENT

Ⓢ Supporting Information

The Supporting Information is available free of charge on the ACS Publications website at DOI: 10.1021/acsami.7b00920.

> Comparison among the experimental Raman spectra of α-AgVO$_3$ obtained at 10, 20, and 30 °C (close-up between 10 and 270 cm^{-1}) (Figure S1); the Wulff crystal representation of optimized α-AgVO$_3$ (Figure S2); and a table summarizing experimental and calculated values of the Raman-active modes listed together with those reported in the literature (Table S1) (PDF)

AUTHOR INFORMATION

Corresponding Author
*E-mail: g.ianeoliveira@hotmail.com.

ORCID Ⓞ
Regiane Cristina de Oliveira: 0000-0002-7332-8731
Marcelo Assis: 0000-0003-0355-5565

REFERENCES

(1) Takeuchi, K. J.; Marschilok, A. C.; Davis, S. M.; Leising, R. A.; Takeuchi, E. S. Silver Vanadium Oxides and Related Battery Applications. *Coord. Chem. Rev.* **2001**, *219-221*, 283−310.

(2) Kittaka, S.; Matsuno, K.; Akashi, H. Crystal Structure of α-AgVO$_3$ and Phase Relation of AgVO$_3$. *J. Solid State Chem.* **1999**, *142*, 360−367.

(3) Kittaka, S.; Yata, Y.; Matsuno, K.; Nishido, H. Interaction of Ag Ions with a Vanadium Pentoxide Hydrate-Formation of Silver Vanadate at Low Temperature. *J. Mater. Sci.* **2000**, *35*, 2185−2192.

(4) Fleury, P.; Kohlmuller, R. Sur le Système Ag$_2$O−V$_2$O$_5$. *C. R. Acad. Sci.* **1966**, *262*, 475.

(5) Rozier, P.; Galy, J. Ag$_{1.2}$V$_3$O$_8$ Crystal Structure: Relationship with Ag$_2$V$_4$O$_{11−y}$ and Interpretation of Physical Properties. *J. Solid State Chem.* **1997**, *134*, 294−301.

(6) Rozier, P.; Savariault, J.-M.; Galy, J. β AgVO$_3$ Crystal Structure and Relationships with Ag$_2$V$_4$O$_{11}$ and δ Ag$_x$V$_2$O$_5$ J. *J. Solid State Chem.* **1996**, *122*, 303−308.

(7) Cheng, F.; Chen, J. Transition Metal Vanadium Oxides and Vanadate Materials for Lithium Batteries. *J. Mater. Chem.* **2011**, *21*, 9841−9848.

(8) Longo, V. M.; De Foggi, C. C.; Ferrer, M. M.; Gouveia, A. F.; André, R. S.; Avansi, W.; Vergani, C. E.; Machado, A. L.; Andrés, J.; Cavalcante, L. S.; Hernandes, A. C.; Longo, E. Potentiated Electron Transference in α-Ag$_2$WO$_4$ Microcrystals with Ag Nanofilaments as Microbial Agent. *J. Phys. Chem. A* **2014**, *118* (31), 5769−5778.

(9) Lemos, P. S.; Altomare, A.; Gouveia, A. F.; Nogueira, I. C.; Gracia, L.; Llusar, R.; Andrés, J.; Longo, E.; Cavalcante, L. S. Synthesis and Characterization of Metastable β-Ag$_2$WO$_4$: An Experimental and Theoretical Approach. *Dalton Trans.* **2016**, *45*, 1185−1191.

(10) Alvarez Roca, R.; Lemos, P. S.; Andrés, J.; Longo, E. Formation of Ag Nanoparticles on Metastable β-Ag$_2$WO$_4$ Microcrystals Induced by Electron Irradiation. *Chem. Phys. Lett.* **2016**, *644*, 68−72.

(11) Li, Y.; Zhang, W.; Niu, J.; Chen, Y. Mechanism of Photogenerated Reactive Oxygen Species and Correlation with the Antibacterial Properties of Engineered Metal-Oxide. *ACS Nano* **2012**, *6*, 5164−5173.

(12) Roca, R. A.; Lemos, P. S.; Gracia, L.; Andrés, J.; Longo, E. Uncovering the Metastable γ-Ag$_2$WO$_4$ Phase: A Joint Experimental and Theoretical. *RSC Adv.* **2017**, *7*, 5610−5620.

(13) de Oliveira, R. C.; Assis, M.; Teixeira, M. M.; da Silva, M. D. P.; Li, M. S.; Andres, J.; Gracia, L.; Longo, E. An Experimental and Computational Study of β-AgVO$_3$: Optical Properties and Formation of Ag Nanoparticles. *J. Phys. Chem. C* **2016**, *120*, 12254−12264.

(14) Pan, G.-T.; Lai, M.-H.; Juang, R.-C.; Chung, T.-W.; Yang, T. C.-K. Preparation of Visible-Light-Driven Silver Vanadates by a Microwave-Assisted Hydrothermal Method for the Photodegradation of Volatile Organic Vapors. *Ind. Eng. Chem. Res.* **2011**, *50*, 2807−2814.

(15) Singh, D. P.; Polychronopoulou, K.; Rebholz, C.; Aouadi, S. M. Room Temperature Synthesis and High Temperature Frictional Study of Silver Vanadate. *Nanotechnology* **2010**, *21*, 325601.

(16) Chen, T.; Shao, M.; Xu, H.; Wen, C.; Lee, S. T. Control over the Crystal Phase, Crystallinity, Morphology of AgVO₃ via Protein Inducing Process. *J. Colloid Interface Sci.* **2012**, *366*, 80−87.

(17) McNulty, D.; Ramasse, Q.; O'Dwyer, C. The Structural Conversion from α-AgVO₃ to β-AgVO₃: Ag Nanoparticle Decorated Nanowires with Application as Cathode Materials for Li-ion Batteries. *Nanoscale* **2016**, *8*, 16266−16275.

(18) Kresse, G.; Hafner, J. Ab Initio Molecular-dynamics Simulation of the Liquid-metal-amorphous-semiconductor Transition in Germanium. *Phys. Rev. B: Condens. Matter Mater. Phys.* **1994**, *49*, 14251−14269.

(19) Perdew, J. P.; Burke, K.; Ernzerhof, M. Generalized Gradient Approximation Made Simple. *Phys. Rev. Lett.* **1996**, *77*, 3865−3868.

(20) Kresse, G.; Joubert, D. From Ultrasoft Pseudopotentials to the Projector Augmented-wave Method. *Phys. Rev. B: Condens. Matter Mater. Phys.* **1999**, *59*, 1758−1775.

(21) Wulff, G. On the Question of Speed of Growth and Dissolution of Crystal Surfaces. *Z. Kristallogr.* **1901**, *34*, 449−530.

(22) Ferrer, M. M.; Gouveia, A. F.; Gracia, L.; Longo, E.; Andrés, J. A 3D Platform for the Morphology Modulation of Materials: First Principles Calculations on the Thermodynamic Stability and Surface Structure of Metal Oxides: Co₃O₄,α-Fe₂O₃, and In₂O₃. *Modell. Simul. Mater. Sci. Eng.* **2016**, *24*, 025007.

(23) Barmparis, G. D.; Lodziana, Z.; Lopez, N.; Remediakis, I. N. Nanoparticle Shapes by Using Wulff Constructions and First-principles Calculations Beilstein. *Beilstein J. Nanotechnol.* **2015**, *6*, 361−368.

(24) Gouveia, A. F.; Ferrer, M. M.; Sambrano, J. R.; Andrés, J.; Longo, E. Modeling the Atomic-scale Structure, Stability, and Morphological Transformations in the Tetragonal Phase of LaVO₄. *Chem. Phys. Lett.* **2016**, *660*, 87−92.

(25) Gurlo, A. Nanosensors: Towards Morphological Control of Gas Sensing Sctivity. SnO₂, In₂O₃, ZnO and WO₃ Case Studies. *Nanoscale* **2011**, *3*, 154−165.

(26) Andres, J.; Gracia, L.; Gouveia, A. F.; Ferrer, M. M.; Longo, E. Effects of Surface Stability on the Morphological Transformation of Metals and Metal Oxides as Investigated by First-principles Calculations. *Nanotechnology* **2015**, *26*, 405703.

(27) Clinical and Laboratory Standards Institute. *Methods for Dilution Antimicrobial Susceptibility Tests for Bacteria That Grow Aerobically- CLSI document M7-A7*, 7th ed.; CLSI: Wayne, PA, 2006.

(28) Zamperini, C. A.; André, R. S.; Longo, V. M.; Mima, E. G.; Vergani, C. E.; Machado, A. L.; Varela, J. A.; Longo, E. Antifungal Applications of Ag-Decorated Hydroxyapatite Nanoparticles. *J. Nanomater.* **2013**, *2013*, 1−9.

(29) André, R. S.; Zamperini, C. A.; Mima, E. G.; Longo, V. M.; Albuquerque, A. R.; Sambrano, J. R.; Machado, A. L.; Vergani, C. E.; Hernandes, A. C.; Varela, J. A.; Longo, E. Antimicrobial Activity of TiO₂:Ag Nanocrystalline Heterostructures: Experimental and Theoretical Insights. *Chem. Phys.* **2015**, *459*, 87−95.

(30) Larson, A. C.; Dreele, R. B. V. *GSAS: General Structure Analysis System*; Los Alamos National Laboratory, 2000.

(31) Kong, X.; Guo, Z.; Zeng, C.; Huang, J.; Cao, L.; Li, L.; Yin, L.; Wen, P.; Feng, Q.; Xu, Z. Soft Chemical in Situ Synthesis, Formation Mechanism and Electrochemical Performances of 1D Bead-like AgVO₃ Nanoarchitectures. *J. Mater. Chem. A* **2015**, *3*, 18127−18135.

(32) Song, J.-M.; Lin, Y.-Z.; Yao, H.-B.; Fan, F.-J.; Li, X.-G.; Yu, S.-H. Superlong β-AgVO₃ Nanoribbons: High-Yield Synthesis by a Pyridine-assisted Solution Approach, Their Stability, Electrical and lectrochemical Properties. *ACS Nano* **2009**, *3*, 653−660.

(33) Bao, S. J.; Bao, Q. L.; Li, C. M.; Chen, T. P.; Sun, C. Q.; Dong, Z. L.; Gan, Y.; Zhang, J. Synthesis and Electrical Transport of Novel Channel-structured β-AgVO₃. *Small* **2007**, *3*, 1174−1177.

(34) Kubelka, P.; Munk, F. Ein Beitrag Zur Optik Der Farbanstriche. *Z. Techn. Phys.* **1931**, *12*, 593−601.

(35) Wood, D. L.; Tauc, J. Weak Absorption Tails in Amorphous Semiconductors. *Phys. Rev. B* **1972**, *5*, 3144−3151.

(36) Konta, R.; Kato, H.; Kobayashi, H.; Kudo, A. Photophysical Properties and Photocatalytic Activities Under Visible Light Irradiation of Silver Vanadates. *Phys. Chem. Chem. Phys.* **2003**, *5*, 3061−3065.

(37) Longo, V. M.; Cavalcante, L. C. S.; Paris, E. C.; Sczancoski, J. L. C.; Pizani, P. S.; Li, M. S.; Andrés, J.; Longo, E.; Varela, J. A. Hierarchical Assembly of CaMoO₄ Nano-Octahedrons and Their Photoluminescence Properties. *J. Phys. Chem. C* **2011**, *115*, 5207−5219.

(38) Kovalenko, M. V.; Manna, L.; Cabot, A.; Hens, Z.; Talapin, D. V.; Kagan, C. R.; Klimov, V. I.; Rogach, A. L.; Reiss, P.; Milliron, D. J.; Guyot-Sionnnest, P.; Konstantatos, G.; Parak, W. J.; Hyeon, T.; Korgel, B. A.; Murray, C. B.; Heiss, A. W. Prospects of Nanoscience with Nanocrystals. *ACS Nano* **2015**, *9*, 1012−1057.

(39) de Oliveira, R. C.; Gracia, L.; Assis, M.; Li, M. S.; Andres, J.; Longo, E.; Cavalcante, L. S. Disclosing the Electronic Structure and Optical Properties of Ag₄V₂O₇ crystals: Experimental and Theoretical Insights. *CrystEngComm* **2016**, *18*, 6483−6491.

(40) Kröger, F. A.; Vink, H. J. Relations between the Concentrations of Imperfections in Crystalline Solids. *Solid State Phys.* **1956**, *3*, 307−435.

(41) Zhang, S.; Ren, L.; Peng, S. Zn₂SiO₄ Urchin-Like Microspheres: Controlled Synthesis and Application in Lithium-Ion batteries. *CrystEngComm* **2014**, *16*, 6195−6202.

(42) Wang, W. H.; Wang, W. Z.; Xu, H. X. A Facile Method for Synthesizing TiO₂ Sea-Urchin-Like Structures and Their Applications in Solar Energy Harvesting. *Chin. Phys. Lett.* **2011**, *28*, 078103.

(43) Han, X. G.; He, H. Z.; Kuang, X. Z. Q.; Zhang, X. H.; Xu, T.; Xie, Z. X.; Zheng, L. S.; Zhou, X. Controlling Morphologies and Tuning the Related Properties of Nano/Microstructured ZnO. *J. Phys. Chem. C* **2009**, *113*, 584−589.

(44) Dalrymple, O. K.; Stefanakos, E.; Trotz, M. A.; Goswami, D. Y. A Review of the Mechanisms and Modeling of Photocatalytic Disinfection. *Appl. Catal., B* **2010**, *98*, 27−38.

(45) Li, Y.; Zhang, W.; Niu, J.; Chen, Y. Mechanism of Photogenerated Reactive Oxygen Species and Correlation with the Antibacterial Properties of Engineered Metal-Oxide Nanoparticles. *ACS Nano* **2012**, *6*, 5164−5173.

(46) Bomio, M. R. D.; Tranquilin, R. L.; Motta, F. V.; Paskocimas, C. A.; Nascimento, R. M.; Gracia, L.; Andres, J.; Longo, E. Toward Understanding the Photocatalytic Activity of PbMoO₄ Powders with Predominant (111), (100), (011), and (110) Facets. A Combined Experimental and Theoretical Study. *J. Phys. Chem. C* **2013**, *117*, 21382−21395.